Simultaneous stereo-PIV and OHxCH2O PLIF measurements in turbulent ultra lean CH4/H2 swirling wall-impinging flames

Luming Fan, Bruno Savard, Spencer Carlyle, Mohammadreza Nozari, Rani Naaman, Benoît Fond, Patrizio Vena

Simultaneous stereo-PIV and OH×CH_2O PLIF measurements in turbulent ultra lean CH_4/H_2 swirling wall-impinging flames

Luming Fan[a,b], Bruno Savard[b], Spencer Carlyle[a], Mohammadreza Nozari[b], Rani Naaman[b], Benoît Fond[c], Patrizio Vena[a,*]

[a] *Aerospace Research Centre, National Research Council, 1200 Montreal Rd., Ottawa, ON K1A 0R6, Canada*
[b] *Department of Mechanical Engineering, Polytechnique Montréal, Montréal, QC H3T 1J4, Canada*
[c] *ONERA - The French Aerospace Lab, 8 rue des Vertugadins, 92190 Meudon, France*

Abstract

We present experimental results from turbulent low-swirl lean H_2/CH_4 flames impinging on an inclined, cooled iso-thermal wall, based on simultaneous stereo-PIV and OH×CH_2O PLIF measurements. By increasing the H_2 fraction in the fuel while keeping Karlovitz number (*Ka*) fixed in a first series of flames, a fuel dependent near-wall flame structure is identified. Although *Ka* is constant, flames with high H_2 fraction exhibit significantly more broken reaction zones. In addition, these high H_2 fraction flames interact significantly more with the wall, stabilizing through the inner shear layer and well inside the near-wall swirling flow due to a higher resistance to mean strain rate. This flame-wall interaction is argued to increase the effective local *Ka* due to heat loss to the wall, as similar flames with a (near adiabatic) ceramic wall instead of a cooled wall exhibit significantly less flame brokenness. A second series of leaner flames were investigated near blow-off limit and showed complete quenching in the inner shear layer, where mean strain rate matches the extinction strain rate extracted from 1D flames. For pure CH_4 flames ($Ka \approx 30$), the reaction zone remains thin up to the quenching point, while conversely for the 70% H_2 flame ($Ka \approx 1100$), the reaction zone is highly fragmented. Remarkably, in all near blow-off cases with CH_4 in the fuel, a large cloud of CH_2O persists downstream the quenching point, suggesting incomplete combustion. Finally, ultra-lean pure hydrogen flames were also studied for equivalence ratios as low as 0.22, and through OH imaging, exhibit a clear transition from a cellular flame structure to a highly fragmented flame structure near blow-off.

Keywords: Hydrogen combustion; low swirl flames; PLIF; heat release rate; stereo-PIV

1. Introduction

Flame wall interaction (FWI) is a key problem in the optimization of all internal combustion devices as it adversely affects overall combustion efficiency [1], the formation of pollutant emissions (e.g, unburnt hydrocarbons, soot) [2], as well as the durability and lifetime of heated components (e.g., combustor liners and turbine blades in gas turbines). FWI has therefore drawn significant interest from engine manufacturers, and this interest is expected to continue to grow as technical innovations to improve engine efficiency (such as downsizing and higher compression ratios) increase charge confinement (by increasing surface-to-volume ratios) and therefore increase the proportion of fuel consumed near walls.

Laser diagnostics are well-suited to probe the highly non-linear mechanisms of FWI as reviewed in [3]. Combined experimental and numerical studies from the Darmstadt group have investigated side-wall FWI, for example [4, 5]. In those studies, flow fields, CO and CO_2 mole fractions, heat release rate (OH and CH_2O distribution), point-wise gas temperature, etc. were measured by a combination of laser diagnostics in a 2D V-flame burner with a water-cooled side wall. Experimentally and numerically derived velocity and temperature fields, flame quenching distance, and CO distribution were compared on the same configuration. A recent study by Zentgraf and co-workers [6] on a low-intensity turbulent V-flame with side-wall quenching revealed the correlation between the flow field and quenching topology: flame structures similar to either head-on or side-wall quenching were identified, and the transition between the two was found to be driven by the near-wall counter clockwise vortex structures, which were also responsible for the correlation between CO_2 and local gas temperatures. Yet, so far these studies were mainly focused on 2D laminar flames or low turbulence flames, and the fuels used were limited to hydrocarbons.

For practical combustion applications such as gas turbines, however, lean combustion with high turbulence is more relevant, where significantly stronger transport can be expected near the wall. Further, current trends towards leaner combustion to reduce emissions of NO_x also raise the question whether very lean fuel/air mixtures will stay unburnt near wall and escape along the streamline inner surface of the combustor. Therefore, the objective of the present study is to investigate FWI for lean and ultra lean turbulent flames near the blow-off limit. We use a model gas turbine low-swirl burner [7, 8] to significantly enhance the flow dynamics against a water-cooled side wall. The interaction between the flow field and flame quenching topology is investigated by simultaneous stereoscopic-particle image velocimetry (stereo-PIV) and OH×CH_2O planar laser induced fluorescence (PLIF). For the fuel composition, due to the forthcoming stringent requirements on carbon neutrality, H_2/CH_4 mixtures at different hydrogen fractions are used. Hydrogen addition greatly extends the upper blow-off limit of low swirl flames [8], such that the swirling wall-impinging flame can be sustained at a lower laminar flame speed and larger Karlovitz number (*Ka*) at higher H_2 fractions. Hydrogen itself also changes the diffusive properties of the mixture and the flame curvature, which may also have an effect on near-wall quenching, as will be presented in this study.

2. Experimental setup

The turbulent flame-wall interaction setup is shown in Fig. 1 which consists of a model gas turbine low-swirl burner (LSB), water-cooled plate, and simultaneous stereo-PIV and OH×CH_2O PLIF diagnostic.

The LSB is described in detail in [8]. It has a 20.2 mm ID central channel and 32.4 mm OD annular swirler with a 40° vane angle. A turbulence generator with 2.32 mm diameter holes and a 56% blockage ratio was used, and the swirl number was 0.473. Reactants CH_4, H_2, and air were fully premixed 2 m upstream of the burner and regulated with Brooks SLA-Series mass flow controllers (accuracy in equivalence ratio and CH_4/H_2 ratio better than 1%).

The fully lifted swirling flame is impinging onto a 60×40 cm^2 water-cooled flat plate. The plate is tilted by 30° relative to the axial y-direction of the flow to suppress beam steering and near-wall reflection, in order to ensure high-quality PLIF measurements, with the laser sheets incident from the unburnt side and parallel to the wall. Compared to the relatively small swirling flame (less than 10 cm in diameter), the plate can be viewed as an infinite, iso-thermal boundary (of interest to potential future simulation work). Selected test cases were repeated using a ceramic plate of the same size to reduce heat loss and thus investigate the effects of different (near adiabatic) boundary conditions.

The horizontal distance between the centre of the burner exit nozzle and the plate was fixed at $L = 2D$ (64 mm) such that with a 30° angle, flames could sufficiently interact with the plate while also allowing sufficient space for the incident laser sheets. The water-cooled plate has a 5 mm thick stainless steel front cover with a measured surface flatness < 15 μm, and an aluminium back with 1 cm deep cooling water channels. The temperature of the plate was measured by an array of thermocouples placed at different depths and axial locations, and by thermal camera imaging directly after the flame was turned off. Both methods indicate that, the plate temperature was stable at roughly 330 K and uniform within 8 K in a 30 cm × 40 cm area which fully covered the flame-interaction zone. The front surface of both plates was painted black to limit unwanted reflections.

Simultaneous stereo-PIV and OH×CH_2O PLIF measurements were obtained using diagnostics previously described in [8]. For the current experiments, the 282.94 nm (OH PLIF), 355 nm (CH_2O PLIF), and 532 nm (stereo-PIV) coincident laser sheets were redirected using a periscope consisting of two broadband mirrors. The light sheets were steered parallel to the wall to minimize undesired reflections.

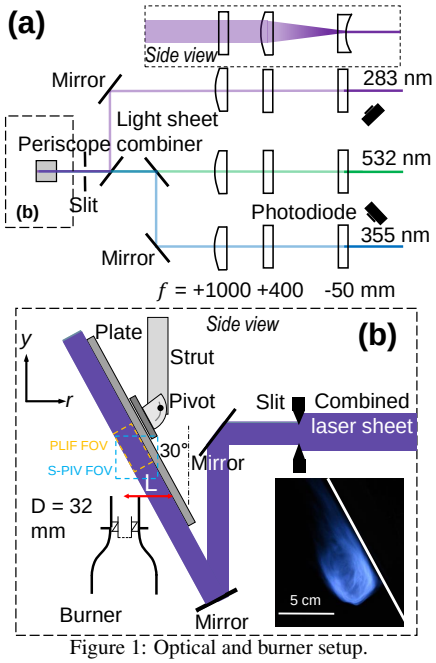

Figure 1: Optical and burner setup.

To reduce the number of readout pixel columns and maximize the image frame rate, two PIMAX 2 PLIF cameras were tilted by 30° so the pixel columns were parallel to the light sheet. This resulted in a 35.2×79.9 cm^2 field of view in the flow with a projected spatial resolution of 87.9 μm/pixel. Raw instantaneous OH and CH_2O images were spatially registered using a target, corrected for background, individual laser pulse energy, mean laser profile, and filtered in Matlab following procedures outlined in [8]. Individual heat release rate (HRR) contours were calculated from the pixel-to-pixel product of the OH and CH_2O images based on the approach of [9] which was further validated for ultra-lean premixed H_2-CH_4/air flames by 1D flame simulations (see supplementary material SM1).

Two Imager sCMOS cameras were used to capture Mie scattering from particles, with a projected spatial resolution of 31.3 μm/pixel. Stereo-PIV vector fields were calculated in Davis 8.4 using a 32×32 interrogation window with 50% overlap, which led to a nominal density of 0.94 mm/vector and apparent vector spacing of 0.47 mm. A specialized calibration target (type 106-10, LaVision) was used to physically map the velocity field and PLIF images. The combined diagnostic system was run at 2 Hz and 500 instantaneous images were acquired for each flame condition.

2.1. Operation conditions

The test conditions are summarized in Table 1 and plotted on a Borghi-Peters diagram in Fig. 2. All cases are premixed. Three groups of data were collected: For cases S1-S4, *Ka* is fixed by keeping the laminar flame speed S_L^0 and flame thickness δ relatively constant for different hydrogen fractions. Case K1 complements S1-S4 with a similar *Ka*, which is realized by running the same 70:30 (X_{H_2}:X_{CH_4}, by mole) fuel composition as in S4, but at a richer equivalence ratio to reduce the flame thickness, while increasing the flow velocity to yield a higher turbulence intensity and thus a smaller Kolmogorov length scale. Cases C1-C4 have the same hydrogen fractions as S1-S4, but at a very lean condition near blow-off. Note the very large *Ka* for C3 and C4. H1 to H5 are ultra-lean H_2/air flames with $\phi = 0.40$ to 0.22 (near blow-off), respectively. For near blow-off flames, the particle seeding necessary for PIV made it difficult to stabilise the flame, whereas PIV measurements are necessary to calculate the local integral length scale l_t and the velocity fluctuation v'. PIV were therefore performed for slightly richer conditions with an 0.01-0.04 increase in equivalence ratio for C1-C4 and H6. This slight change of stoichiometry is expected to have a negligible impact on the velocity field on the unburnt side where *Ka* were estimated. For the other cases, instantaneous velocity field was acquired simultaneously with PLIF images. The local Karlovitz number was estimated by $Ka = (l_t/\delta)^{-1/2} v'/S_L^0)^{3/2}$ [10], where v' is the three-component rms velocity, δ the laminar flame thickness, and S_L^0 the laminar flame speed. An example calculation for l_t and *Ka* is presented in supplementary material SM2.

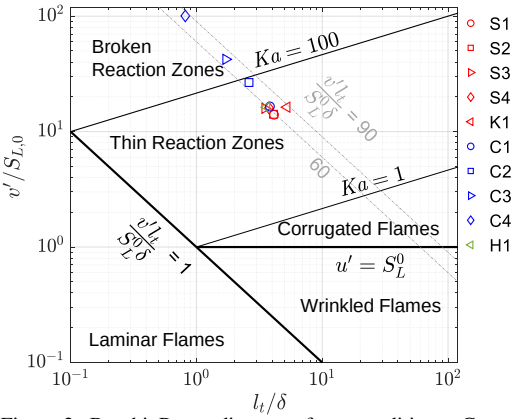

Figure 2: Borghi–Peters diagram of test conditions. Cases H2-5 are not shown as flame speed calculations cannot converge for those cases.

3. Results and discussion

3.1. Flow fields

Figure 3 shows the mean and rms velocity fields of the impinging swirling reacting flow for reference 100% CH4 condition S1 and 30% CH4 / 70% H2 condition S4. For all test cases, the uncertain of velocity measurement was below (0.1, 0.06, 0.3) m/s for x, y, and z components respectively, calculated in Davis 8.4. The progress variable $\bar{c}$ = 0.1, 0.5, and 0.9 are

Table 1: A summary of test conditions.

Case	v'/V (m/s)	ϕ	X_{H_2}:X_{CH_4}	S_L^{0*} (cm/s)	δ^* (mm)	Re_T	Le_{eff} **	Ka***
S1	2.2/10	0.65	0:100	15.43	0.78	460	1.01	26
S2	2.1/10	0.60	30:70	15.00	0.79	453	0.88	27
S3	2.2/10	0.55	50:50	13.90	0.84	428	0.78	34
S4	2.2/10	0.50	70:30	13.76	0.84	462	0.67	34
K1	3.3/15	0.55	70:30	20.33	0.64	734	0.70	29
C1	2.2/10	0.62	0:100	13.08	0.88	482	1.01	36
C2	2.2/10	0.52	30:70	8.23	1.26	477	0.86	85
C3	2.2/10	0.45	50:50	5.13	1.84	451	0.74	212
C4	2.1/10	0.37	70:30	2.06	4.03	449	0.61	1124
H1-H5****	2.6-2.2/10	0.40-0.22	100:0	15.98 - $<$ 3.01	0.77 - $>$ 2.92	479-448	0.47 - $<$0.43	29 - $>$ 200

* Calculated in Cantera using GRI-Mech 3.0. ** Calculated following the approach described in [10]. *** A global *Ka* was estimated using the integral length scale l_t in the swirling flow averaged over a 5×5 mm square area marked in Fig. 3(a). l_t in the swirling flow is between 3.2-3.4 mm for all cases. **** Cantera failed to provide converging results for H_2 flames below $\phi = 0.32$. At 0.33, *Ka* = 170, so *Ka* in H2-H5 are expected to be well above 200.

also plotted on the mean velocity field to highlight the flame position relative to the swirling flow and the side wall, derived from the ensemble average of binarized OH images. In both Fig. 3(a) and (c), the bottom of the images at a height above the burner HAB = 40 mm shows the relatively lower velocity in the central flow between radial positions $r = 0$ to 10 mm surrounded by the higher velocity swirling flow near $r \approx 20$ mm, which is typical of low-swirl flames. In Fig. 3(a), the progress variable iso-contours show the mean flame position of S1 is effectively shrouded by the inner shear layer, such that the flame remains several millimetres from the wall. Conversely, Fig. 3(c), the mean flame position clearly crosses the shear layer and stabilizes closer to the wall, and leads to a strong downstream acceleration from thermal expansion.

In both Fig. 3(b) and (d), velocity fluctuations are dampened after impingement and a recirculation zone is formed at the right bottom corner. This recirculation zone does not occur without the presence of the wall (see the previous unconfined study using the same LSB [8]) and further helps stabilize the flame. Comparing with values listed in Table 1, the inclined side wall extended the leanest flammability by roughly 0.14-0.18 for the same hydrogen fractions as C1-C4 and H5. A LES study by [11] also reported the conducive effect of the side plate for flame stabilization may be attributed to the recirculation zone generated by the interaction between the swirling flow motion and a side wall. Another contributing factor could be that the semi-confinement prevents strong entrainment of cold air.

Karlovitz number iso-contours, plotted on the rms velocity field, in addition to mean strain rate iso-contours calculated based on the in-plane gradient of the mean velocity field (not shown in Fig. 3), will help analyse the flame structure in the following sections.

3.2. FWI at constant Karlovitz number

Figure 4 shows single shot OH and CH_2O images and the normalised HRR distribution derived from their product, for cases S1-S4[a] and K1, which all have

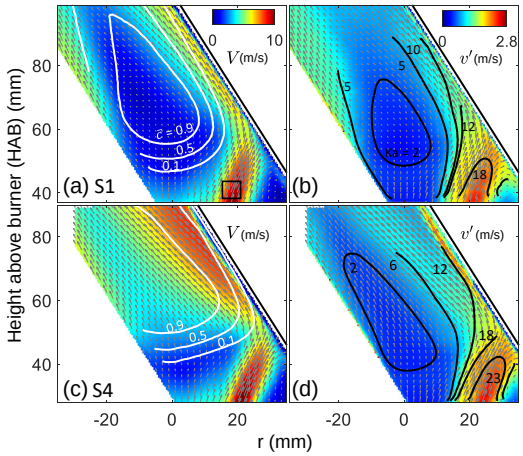

Figure 3: Mean (left) and RMS (right) velocity fields for S1 and S4. The white lines are the progress variable $\bar{c} = 0.1$, 0.5, and 0.9, obtained by averaging binarized OH images, which mark the instantaneous position of the flame front. The black curves are the *Ka* iso-contour calculated based on the local l_t and v'. The black square in (a) highlights the region where the global *Ka* in Table 1 are estimated.

similar *Ka*. The images were rotated such that the wall lays horizontally 1.2 mm beneath the bottom of the images. As the flame position changed slightly among cases, the field of view is adjusted by moving the burner relative to the fixed cameras. We plot *Ka* iso-contours on the OH images, mean in-plane strain rate contours corresponding to the mean extinction strain rate (ESR) on the CH_2O images, and simultaneous velocity vectors and mean progress variable iso-contours on the HRR field. Several observations are made as follows.

First, visual inspection of the leading edge of the instantaneous flame images in the far-wall region shows enhanced wrinkling in the OH distributions that gradually becomes more pronounced from flames S1 to S4-K1 as the fraction of H_2 in the fuel increases,

[a]Complete figures of the example single-shots including cases S3, C3 and H2,4 are in supplementary material 3.

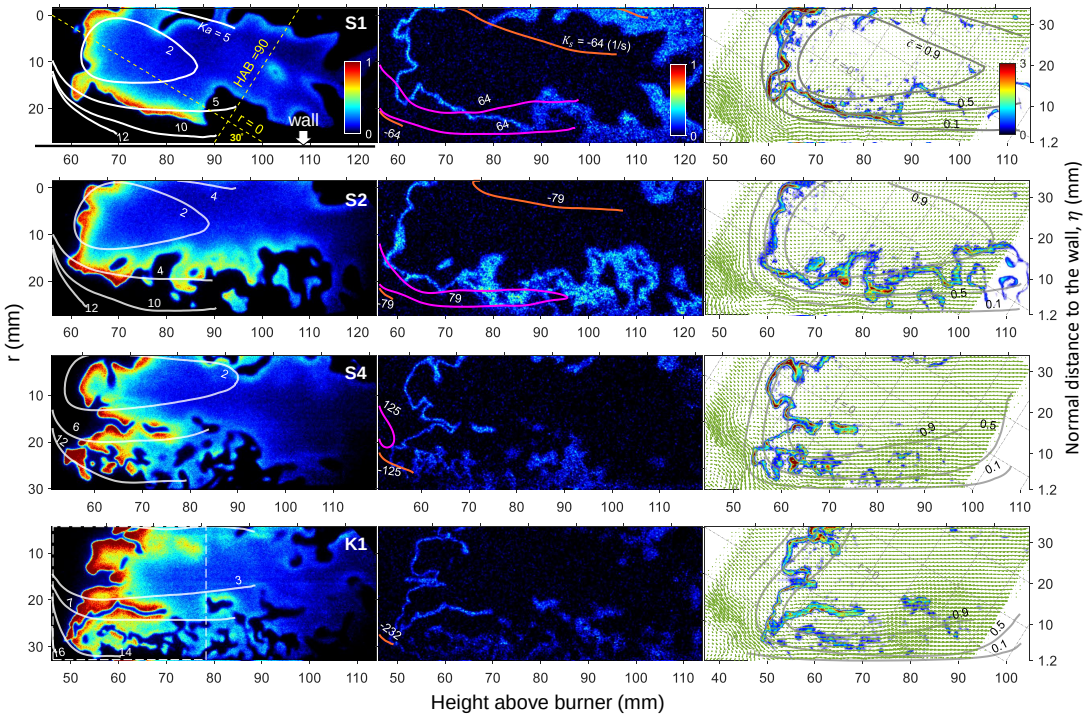

Figure 4: Example OH (left), CH_2O (middle), and the simultaneous velocity field superimposed by calculated HRR (right) images for cases S1-K1 at a near constant laminar flame speed S_L^0. The left and bottom ticks mark the Cartesian coordinate defined by r and HAB at 30° with the wall, as illustrated by the yellow dotted lines in S1. The ticks on the right side of the HRR images denote the normal distance to the wall. The range of axes in the HRR images are sightly shifted to reveal the velocity vectors in the swirling region upstream the flame front. The dashed rectangle on the OH image of K1 marks the region where local flame curvature and HRR are calculated for Figs.5 and 6. Contours of *Ka*, mean in-plane strain rate corresponding to ESR, and reaction progress variables are plotted on OH, CH_2O, and HRR images, respectively. The scale is the same in all subfigures.

as has been confirmed for H_2 addition in a low swirl burner [12]. The occurrence of these cellular structures is caused by thermo-diffusive instability and the competing thermal and mass diffusivities of the deficient reactant (H_2) [13]. As Le_{eff} decreases with H_2 in the fuel, the relatively higher mass diffusivity of H_2 enhances positively curved flame regions and effectively starves negatively curved flame regions. A positive correlation between HRR and curvature [14] can indeed be observed (right column) for these cases, which is confirmed in Fig. 5 where the joint PDFs of HRR and curvature are presented for various wall distances. This correlation is particularly strong away from the wall, while it essentially disappears near the wall, where *Ka* is largest. Using direct numerical simulations (DNS), Aspden *et al.* [15] observed a decorrelation between heat release rate and curvature in hydrogen flames as *Ka* increased in the range $\mathcal{O}(10)$–$\mathcal{O}(100)$, which may relate to the latter observation.

Second, there is a fuel composition effect on the flame stabilization location. At fixed *Ka* and S_L^0, as the H_2 fraction increases, the turbulent flame speed is expected to increase [16], which leads to the flame stabilizing further upstream and into the near-wall high velocity region (Note the shift in plotted HAB locations among the five cases to better visualise the flame). Note that for case K1, the velocity field differs due to the higher bulk flow velocity (15 m/s vs. 10 m/s), and, because of the larger turbulent Reynolds number, the turbulent to laminar flame speed ratio is expected to be larger than case S4 [17].

Third, unlike the quenching topology shown in [6], here close to the wall the OH distribution is highly broken for the high hydrogen fraction cases (S4 and K1) and is associated with broadening of the CH_2O layer as well as a broken/distributed reaction zone. These PLIF results are consistent with the DNS results obtained in [16]: at fixed *Ka* and l_t/δ, the reaction zone of hydrogen flames is much more broken/distributed than that of methane flames. According to that study, such brokenness is due to "the thermodiffusively-unstable behaviour of hydrogen", which is exaggerated by turbulence, "creating small-scale structures with higher curvature than at lower *Ka*, resulting in more intense burning over a broad flame brush." This is further illustrated by the standard deviation (width) of the curvature PDFs shown in Fig. 6. Closer to the wall where *Ka* is largest, the hydrogen flame curvature distribution is significantly broadened (cases S4 and K1). However, for the

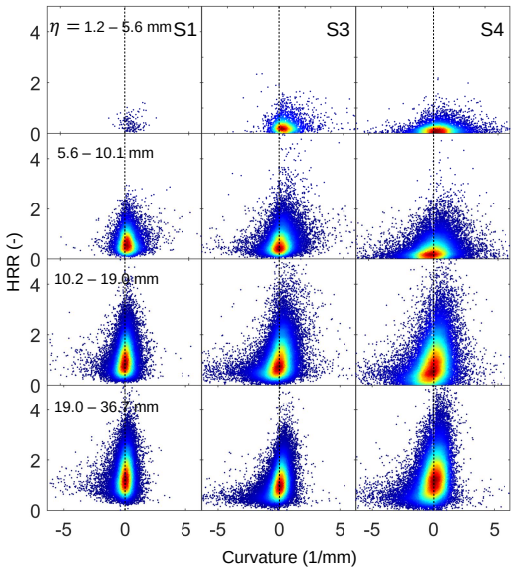

Figure 5: Joint PDF of local HRR peak along the flame front (discretized with fixed curvilinear length) versus local flame curvature, conditioned by the wall distance. The HRR was normalized by its 97 percentile value in that frame. The region of data extraction is shown in Fig. 4 (dashed rectangle).

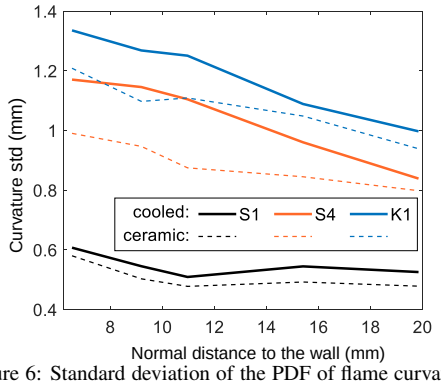

Figure 6: Standard deviation of the PDF of flame curvature collected at different distances to the wall for S1, S4, K1.

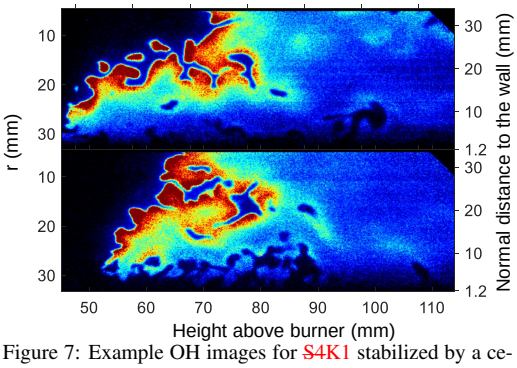

Figure 7: Example OH images for ~~S4~~K1 stabilized by a ceramic plate. The color scale is adjusted to best display the near wall region where the OH signal is weak.

methane flame S1, no obvious change in the curvature distribution is observed. Consistent with results obtained in turbulent counterflow H_2/CH_4 flames [18], the standard deviation of curvature PDF is significantly increased with increased hydrogen fraction.

Fourth, close to the wall, the reaction zone for the H_2/CH_4 flames is highly broken, more than could be expected for a *Ka* of order 10. It is possible that the local *Ka* is significantly larger as a result of enthalpy loss to the wall (leading to lower flame speed and larger flame thickness). Since in cases S4 and K1, highly fragmented OH signal has reached the bottom edge of the image, at such a small distance from the wall (1.2 mm) the local heat flux to the wall is expected to be non-negligible. The reduction of mean OH $\times$ CH_2O magnitude at zero curvature when approaching the wall (shown in Fig. 5) further suggests the reaction may be suppressed due to heat loss. To verify this hypothesis, Fig. 7 compares the flame OH PLIF measurements for case K1 with a flame at the same conditions, but with the cooled wall replaced by a (nearly adiabatic) ceramic wall. Since the ceramic plate surface is not as fine as its stainless steel counterpart, and that some deformation might happen during the measurements, the OH signals within 3 mm from the wall were not captured. Yet, it can still be clearly seen that for most of single frames (first row) the flame front is much less broken along the wall, showing a typical side-wall quenching topology where a curved flame front is flattened by the wall (laminarization) [3]. A broken flame front only appears occasionally (second row in Fig. 7) at about 1 out of 20 snapshots frequency and regionally below 90 mm HAB due to the stochastic nature of turbulent flames and possibly the swirling motion that transport broken pockets of OH from outside the plane. Figure 6 confirms the wider distribution of flame front curvature near the cooled wall compared to that near the ceramic wall.

Finally, the mean extinction strain rate (ESR) for each flame is calculated in Cantera using a 1D impinging flame configuration assuming 330 K wall temperature. For S1-S4 and K1, the ESR obtained are 64, 79, 87, 125, and 232 (1/s), respectively. The mean strain rate iso-contours corresponding to these values are included in the CH_2O PLIF images. It can be noted that the main (persistent) strain rate is below the ESR almost everywhere for cases S3, S4, and K1. These flames penetrate well into the shear layer near the wall and quench apparently due to direct flame-wall interaction, as shown by the instantaneous flame-velocity interaction in Fig 4. For example, in S4, the flame front has entered the swirling flow and been stretched. For case S1 (and S2 to a lesser extent), there is a non-negligible region within which persistent strain rate exceeds the ESR, which is likely to explain the apparent flame quenching at HAB $\approx$ 100 mm (case S1). Note that premixed turbu-

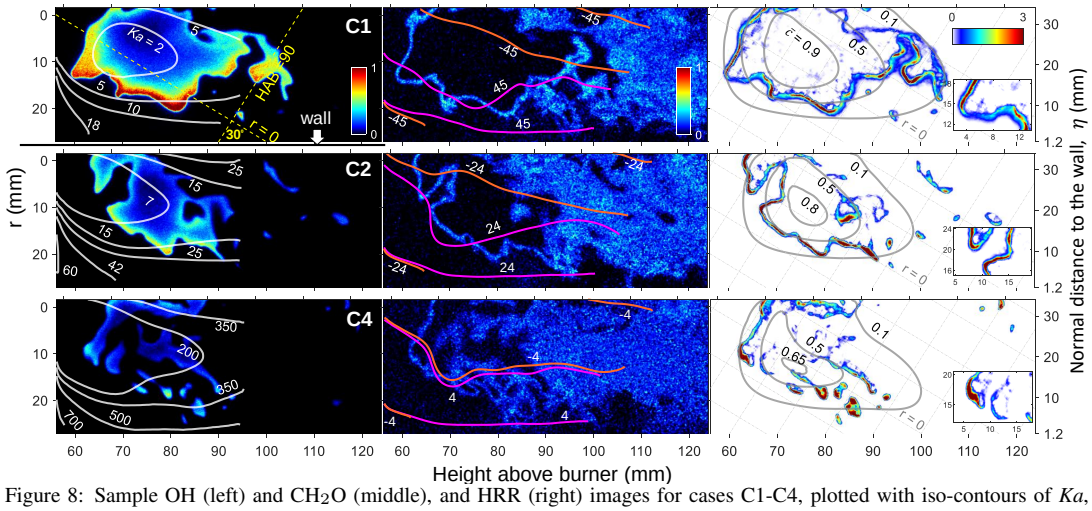

Figure 8: Sample OH (left) and CH_2O (middle), and HRR (right) images for cases C1-C4, plotted with iso-contours of *Ka*, extinction strain rate (1/s), and the progress variable $\bar{c}$, respectively.

lent CH_4 jet flames have been shown to be well modeled (in the mean sense) by 1D counterflow laminar flames with strain rate matching the mean (persistent) strain rate in the turbulent jet flame [19].

Overall, a high mean strain rate (HOQ), persistent heat loss to the wall (SWQ) and the relatively high turbulence provided by the swirling flow together contribute to the unique broken flame structures observed in this inclined wall configuration, which can hardly be conjectured solely from studying each single quenching mechanism.

3.3. Near blow-off limit

Results from the previous section show that, even at moderate nominal *Ka*, the structure of H_2/CH_4 flames is highly disrupted near the wall. Here, we consider the near blow-off cases, which are associated with significantly larger nominal *Ka* (see Table 1).

Figure 8 shows single shot OH, CH_2O, and calculated HRR images for C1-C4. The OH PLIF and HRR images reveal a flame structure highly dependent on fuel composition. The pure CH_4 case (C1) exhibits a highly corrugated, yet continuous and thin flame front. As the H_2 fraction increases (cases C2 to C4), a continuous, corrugated thin flame front persists at the leading edge, but it is followed downstream by an increasingly broken flame front. It is very likely that the increasingly high *Ka* (from 36 up to 1124) with increasing hydrogen fraction at near blow-off limit is responsible for the observed structures.

For all four cases, the flame quenches at HAB $\approx$ 80–90 mm. This quenching is likely not caused by the heat loss to the wall, as the PLIF images for the ceramic plate (shown in supplementary material SM4) exhibit the same behaviour. Quenching downstream is likely due to a high local persistent strain rate that exceeds the extinction strain rate (ESR) under such lean conditions. For C1-C4, the mean ESR obtained from 1D calculations are 45, 23, 13, and 4 (1/s). As shown on the CH_2O PLIF images, for all three cases, the flame quenching region coincides with the region where persistent strain rate is larger than the mean ESR value. Note that, due to their thermo-diffusively unstable nature, 3D H_2 flames are expected to be more resistant to persistent strain rate than 1D flames, such that the ESR may be underestimated from 1D calculations.

The CH_2O PLIF images reveal a unique feature for these ultra lean flames: downstream the flame quenching a wide cloud of CH_2O persists throughout the PLIF field of view. Note that the CH_2O signal is dependent on temperature [20], which was not measured here, such that we cannot conclude if the CH_2O concentration in this cloud increases or decreases downstream. That stated, this cloud is likely due to incomplete combustion of CH_4 originated from the swirling flow. Downstream transport of radicals and intermediates in a very high *Ka* CH_4 premixed jet flame has been observed through DNS [19]. It was argued that, as the flame anchored in a strongly sheared layer, species found in the preheat zone experienced a sufficiently short residence time to be transported downstream without being fully reacted to complete the oxidation process. A similar situation may be encountered here in the quenching region (refer to Fig. 3 for the mean flow field). Incomplete combustion of ammonia due to flame interaction with an uninsulated wall in swirling flames has been recently identified experimentally [21]. Another possibility is that the CH_2O is produced locally. Further high fidelity DNS studies may provide more insights on the origin of the CH_2O cloud.

All flames presented were stabilized steadily, such that structures shown here are not due to transient phenomena during blow-off. To the authors' knowledge, this is the first time such highly fragmented OH distribution and diffused CH_2O are reported. The

CH_2O is not only broadened as observed in a previous high *Ka* experimental jet flame study [22], but forms a large cloud downstream of the quenching point.

3.4. Pure hydrogen flames

Similar highly broken reaction zones can also be observed from H_2/air flames as shown in Fig. 9. A clear transition can be observed from the OH image as *Ka* increases. A complete set of example instantaneous images for all H cases is presented in supplementary material SM3. For ϕ = 0.4 ($Ka = 29$), a cellular flame front characteristic of thermo-diffusive instabilities is seen. From ϕ = 0.26 to 0.22 (*Ka* is unknown due to unresolved laminar flame speed, but should be far beyond 200), the spot-like OH fragments start to appear, first in the near wall region (see H4), then gradually move to the cone region as the mixture goes further leaner (H5). For the leanest condition at ϕ = 0.22, the entire flame becomes highly fragmented. This structure can be compared with that from a DNS of a statistically planar H_2 flames at $\phi = 0.31$ and $Ka = 1562$, which, consistently, exhibited a fragmented reaction zone [23].

3.5. Role of thermal boundary condition

We present the differences in the flame leading edge position for the two plates in Fig. 10. A set of example single-shot images taken with the ceramic plate is also shown in supplementary material SM4, plotted with $\bar{c}$ iso-contours for both plates, comparing the flame structure under different thermal boundary conditions. For cases S3-K1, H1-H2, the leading edge of the flame with the ceramic wall clearly moved upstream. The largest difference is found with S4: with the ceramic plate, the flame enters the swirling flow and presents a different shape compared with the cooled plate counterpart, as illustrated by the images shown in SM4. This is attributed to a higher flame speed near a hot wall ($>$ 500 K measured by an IR camera). Similar behavior has also been observed in a previous study on V-shape flame SWQ with elevated wall temperatures [24]. For cases C2-C4, and H3-H5, however, the flame stabilized further from the wall, such that enthalpy loss and its lowering effect on flame speed is likely negligible. The overlaid iso-contours in C cases in supplementary material SM4 show indeed no difference in the flame structure, regardless which thermal boundary condition is applied.

The wall starts to show an effect on the flame from roughly 3 mm (K1) to 9 mm (S1) based on the mean flame brush position marked by $\bar{c}$ iso-contours. Previous experimental FWI studies concluded the quenching Peclet number P_e (quenching distance normalized by diffusive flame thickness) was 2.6-2.9 for HOQ, and about 7 for SWQ, as summarized in [25]. Unlike previous FWI studies which focused on laminar or moderately turbulent flames near stoichiometry, here *Ka* is large. Hence we use the flame brush thickness (about 10 mm estimated from the $\bar{c}$ between 0.1 to 0.9) to normalized the quenching distance for P_e, instead of using the diffusive flame thickness, leading to $P_e \sim \mathcal{O}(1)$, consistent with previous studies.

4. Conclusions

A model gas turbine low-swirl burner with an inclined iso-thermal wall was used to investigate the flame-wall interaction at lean and ultra lean conditions, for various H_2/CH_4 fuel compositions. The main conclusions are summarized as follows: 1) For constant S_L^0 and *Ka*, increasing hydrogen in the fuel leads to a broken reaction zone near the wall, which is attributed to both the thermo-diffusive instability of hydrogen at low Le, and a high local *Ka* due to heat losses to the wall. This is evidenced by significant broadening of flame curvature PDFs near the wall, a correlation (decorrelation) of curvature with HRR away from (near) the wall, and a systematic increase in reaction zone brokeness/wrinkling when comparing the results obtained with the cooled iso-thermal and near adiabatic walls at the same conditions. 2) At near blow-off conditions, the reaction zone becomes increasingly broken with a lower sustainable flame speed achieved by using higher hydrogen fractions, coinciding with an increase in *Ka* from 36 to 1124. Severe quenching is observed downstream for the near blow-off conditions, likely caused by a strong persistent local strain rate. Remarkably, a large cloud of CH_2O forms beyond this quenching point, possibly resulting from incomplete combustion. 3) A transition from cellular to highly broken flame structures is also observed in hydrogen/air flames as the mixture goes from lean ($\phi = 0.4$) to ultra-lean near-blow off ($\phi = 0.22$). The results reported in the present study are central to the continued development of fuel flexible and H_2 specific aero and heavy frame gas turbines, as we look to transition to zero carbon energy.

Acknowledgments

The authors gratefully acknowledge the financial support from the NRC Aerospace Futures Initiative and Low Emission Aviation Program, and the Natural Sciences and Engineering Research Council of Canada (funding reference numbers RGPIN-2019-04309, RGPAS-2019-00131), the useful discussions with Dr. Marc Day (NREL), and the technical support from Mart J. Regalado and Yin Yang (NRC).

References

[1] F. Foucher, S. Burnel, C. Mounaïm-Rousselle, Evaluation of burning rates in the vicinity of the piston, in a spark-ignition engine, Proc. Combust. Inst. 29 (2002) 12.

[2] A. C. Alkidas, Combustion-chamber crevices: The major source of engine-out hydrocarbon emissions under fully warmed conditions, Prog. Energy Combust. Sci. 25 (3) (1999) 253–273.

[3] A. Dreizler, B. Böhm, Advanced laser diagnostics for an improved understanding of premixed flame-wall interactions, Proc. Combust. Inst. 35 (1) (2015) 37–64.

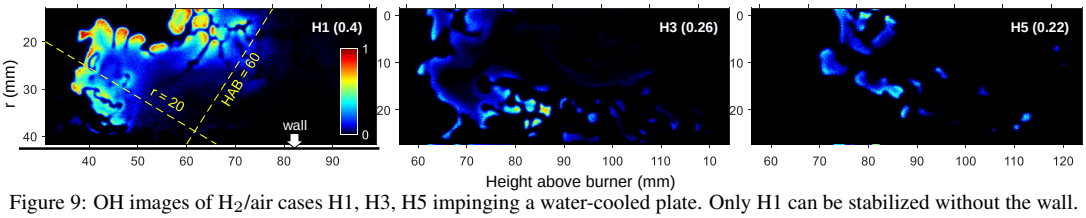

Figure 9: OH images of H_2/air cases H1, H3, H5 impinging a water-cooled plate. Only H1 can be stabilized without the wall.

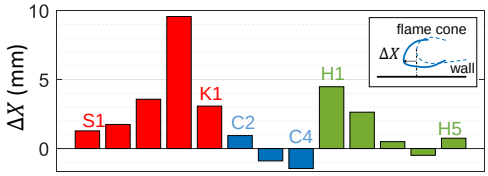

Figure 10: Differences in the flame leading edge position for the two plates. Positive values correspond to an upstream position for the flame with the ceramic plate. The flame with the ceramic plate in C1 was mildly richer than its cooled plate counterpart due to a slightly varied blow-off limit, hence C1 is not presented here.

[4] H. Kosaka, F. Zentgraf, A. Scholtissek, C. Hasse, A. Dreizler, Effect of Flame-Wall Interaction on Local Heat Release of Methane and DME Combustion in a Side-Wall Quenching Geometry, Flow Turbul. Combust. 104 (4) (2020) 1029–1046.

[5] S. Ganter, A. Heinrich, T. Meier, G. Kuenne, C. Jainski, M. C. Rißmann, A. Dreizler, J. Janicka, Numerical analysis of laminar methane–air side-wall-quenching, Combust. Flame 186 (2017) 299–310.

[6] F. Zentgraf, P. Johe, A. D. Cutler, R. S. Barlow, B. Böhm, A. Dreizler, Classification of flame prehistory and quenching topology in a side-wall quenching burner at low-intensity turbulence by correlating transport effects with CO2, CO and temperature, Combust. Flame (2021) 111681.

[7] M. Day, S. Tachibana, J. Bell, M. Lijewski, V. Beckner, R. K. Cheng, A combined computational and experimental characterization of lean premixed turbulent low swirl laboratory flames II. Hydrogen flames, Combust. Flame 162 (5) (2015) 2148–2165.

[8] Q. An, S. Kheirkhah, J. Bergthorson, S. Yun, J. Hwang, W. J. Lee, M. K. Kim, J. H. Cho, H. S. Kim, P. Vena, Flame stabilization mechanisms and shape transitions in a 3D printed, hydrogen enriched, methane/air low-swirl burner, Int. J. Hydrog. Energy 46 (27) (2021) 14764–14779.

[9] P. H. Paul, H. N. Najm, Planar laser-induced fluorescence imaging of flame heat release rate, Proc. Combust. Inst. 27 (1) (1998) 43–50.

[10] N. Peters, Turbulent Combustion, Cambridge Monographs on Mechanics, Cambridge University Press, 2000.

[11] S. Herff, K. Pausch, S. Loosen, W. Schröder, Impact of non-symmetric confinement on the flame dynamics of a lean-premixed swirl flame, Combust. Flame (2021) 111701.

[12] K. Kaufman, M. Emadi, A. Ratner, Effect of hydrogen addition to methane fuel in a low swirl burner, 8th US National Combustion Meeting, 2013 (#070IC-0332).

[13] J. B. Bell, R. K. Cheng, M. S. Day, I. G. Shepherd, Numerical simulation of lewis number effects on lean premixed turbulent flames, Proc. Combust. Inst. 31 (1) (2007) 1309–1317.

[14] M. S. Day, X. Gao, J. B. Bell, Properties of lean turbulent methane-air flames with significant hydrogen addition, Proc. Combust. Inst. 33 (1) (2011) 1601–1608.

[15] A. Aspden, M. Day, J. Bell, Turbulence-chemistry interaction in lean premixed hydrogen combustion, Proc. Combust. Inst. 35 (2) (2015) 1321–1329.

[16] A. J. Aspden, M. S. Day, J. B. Bell, Towards the distributed burning regime in turbulent premixed flames, J. Fluid Mech. 871 (2019) 1–21.

[17] H. Guo, B. Tayebi, C. Galizzi, D. Escudié, Burning rates and surface characteristics of hydrogen-enriched turbulent lean premixed methane–air flames, Int. J. Hydrog. Energy 35 (20) (2010) 11342–11348.

[18] E. Abbasi-Atibeh, J. M. Bergthorson, Differential diffusion effects in counter-flow premixed hydrogen-enriched methane and propane flames, Proc. Combust. Inst. 37 (2) (2019) 2399–2406.

[19] H. Wang, E. R. Hawkes, B. Savard, J. H. Chen, Direct numerical simulation of a high Ka CH4/air stratified premixed jet flame, Combust. Flame 193 (2018) 229–245.

[20] D. C. Kyritsis, V. S. Santoro, A. Gomez, The effect of temperature correction on the measured thickness of formaldehyde zones in diffusion flames for 355 nm excitation, Exp. Fluids 37 (5) (2004) 769–772.

[21] E. C. Okafor, M. Tsukamoto, A. Hayakawa, K. A. Somarathne, T. Kudo, T. Tsujimura, H. Kobayashi, Influence of wall heat loss on the emission characteristics of premixed ammonia-air swirling flames interacting with the combustor wall, Proc. Combust. Inst. 38 (4) (2021) 5139–5146.

[22] B. Zhou, C. Brackmann, Z. Li, M. Aldén, X. S. Bai, Simultaneous multi-species and temperature visualization of premixed flames in the distributed reaction zone regime, Proc. Combust. Inst. 35 (2) (2015) 1409–1416.

[23] A. J. Aspden, M. S. Day, J. B. Bell, Turbulence-flame interactions in lean premixed hydrogen: Transition to the distributed burning regime, J. Fluid Mech. 680 (2011) 287–320.

[24] H. Kosaka, F. Zentgraf, A. Scholtissek, L. Bischoff, T. Häber, R. Suntz, B. Albert, C. Hasse, A. Dreizler, Wall heat fluxes and CO formation/oxidation during laminar and turbulent side-wall quenching of methane and DME flames, Int. J. Heat Fluid Flow 70 (2018) 181–192.

[25] T. Zirwes, T. Häber, F. Zhang, H. Kosaka, A. Dreizler, M. Steinhausen, C. Hasse, A. Stagni, D. Trimis, R. Suntz, H. Bockhorn, Numerical Study of Quenching Distances for Side-Wall Quenching Using Detailed Diffusion and Chemistry, Flow Turbul. Combust. 106 (2) (2021) 649–679.